Stability analysis of hypersonic flow over a backstep in chemical equilibrium

By J.M. Perez†, J.A. Franco‡, P. Paredes¶, S. Hein‡, V. Hannemann‡
AND V. Theofilis†

Universidad Politécnica de Madrid, Madrid, Spain

The purpose of this work is to shed light on the role of chemical equilibrium in the global instabilities that arise in hypersonic non-parallel flows. As an example of separated flow, the stability of temporally evolving disturbances on a hypersonic flow over a backstep are examined by solution of the pertinent BiGlobal eigenvalue problem. The flow conditions are unit $Re' = 6.6 \times 10^6$ 1/m, boundary-layer edge temperature 350 K and freestream Mach=10. The step height is taken to equal to the local displacement thickness. At these conditions the two-dimensional laminar base flow is computed with the full Navier-Stokes DLR-TAU solver.

Stability results at a given wave number of the perturbations in the homogeneous direction show that the leading linear mode located around the recirculation bubble is unstable to modal perturbations when both perfect and real gas assumption is made. Real gas effects increase the temporal growth rate of the leading mode, which corresponds to a zero-frequency three-dimensional global linear instability, the analog of which in incompressible flow is well understood. The eigenvalue spectrum and the structure of the leading mode for real and perfect gas are compared.

1. Introduction

Reentry vehicles are exposed to severe flow conditions as high heat loads. Therefore they require the use of thermal protection. This implies complex thermo-chemical processes that affect the heat flux on the body surface. Due to the lack of knowledge about the origin of laminar-turbulent transition on parts of the vehicle surface, or the underlying instabilities, very often this protection is oversized, implying an unnecessary excess weight and consequent performance reduction. Given the high temperatures reached on the body surface, where the boundary layer develops, experimental studies are prohibitively expensive and one resorts to numerical simulations which provide information about the physical process involved in laminar-turbulent transition. Turbulence leads to larger heat fluxes than a laminar boundary layer due to the increased convective transport and has a strong influence in the drag, thermal load and stability and therefore the accurate prediction of this is a critical part of the aerodynamic design of hypersonic vehicles. As conclusion, the study of laminar-turbulent transition in supersonic and hypersonic boundary layers is important in the development of next generation of hypersonic vehicles.

† josemiguel.perez@upm.es
‡ DLR Göttingen, Germany
¶ Computational AeroSciences Branch, NASA Langley Research Center, Hampton, VA, USA

However, hypersonic flows have attracted much less attention in the literature with respect to laminar-turbulent flow transition, partly because of the complexity of the flow fields involved, since at high temperature conditions, chemical reactions need to be taken into account. Specifically the authors are not aware of any global instability study at hypersonic flow conditions. In increasing temperature order, four possible flow regimes exist: (a) At moderately high temperatures the air is a mixture of perfect gases. (b) When the temperature increases the gas is a mixture of species at chemical and thermal equilibrium. (c) The next flow regime chemical equilibrium is broken but thermal equilibrium assumption still holds. (c) At high temperatures both thermal and chemical equilibrium are not met.

Efforts that have applied classic linear instability analysis in order to arrive at predictions on small-amplitude perturbation growth and correlate such results with transition location at hypersonic flight speeds and accounting for real gas effects are limited to one-dimensional, boundary-layer type of basic flows [7, 8, 14].

Using direct numerical simulations Mack [5] determined that whenever the relative flow between the mean flow and the disturbance phase velocity is supersonic, a family of inviscid acoustic disturbances at high frequency exists. The first of the higher frequency modes is known in the literature as the second mode or the Mack mode. Later, Mack [6] arrived to the following results for hypersonic flat-plate boundary layer transition using linear stability theory: oblique three-dimensional viscous disturbances are dominant at all supersonic Mach numbers below four which is an extension to high speeds of the Tollmien-Schlichting instability, while a family of trapped high frequency acoustic modes traveling inside the boundary layer by reflections between the wall and the sonic line dominates at high Mach numbers. The acoustic instability discovered by Mack arises when the edge velocity is sufficiently fast that disturbances can propagate downstream at a subsonic speed relative to the boundary-layer edge velocity but supersonic relative to the wall. This second instability was measured in different experiments, [2], [4] or [13] and becomes more unstable that the first oblique mode for free-stream Mach numbers bigger than four.

The study of these modes was recovered later by Malik [7] and Malik and Anderson [8], who conducted the stability analysis of a zero-pressure-gradient flat plate boundary layer at hypersonic regime including real gas at thermal and chemical equilibrium. These authors were the first to calculate the real gas effects on hypersonic boundary layer stability. For this end they studied two cases at Mach numbers, 10 and 15, and found that the effect of considered real gas produce large differences in the temperature profile in the boundary layer. They show that chemical equilibrium stabilizes the first oblique mode and destabilizes the second mode. In this case, the size of the region of relative supersonic flow increases in the cooler boundary layer, due to the lower speeds of sound in that region. In addition, the second mode is shifted to lower frequencies. Later Stuckert and Reed [14] studied the effect of chemical non-equilibrium on flow over an axisymmetric cone.

By contrast, when the basic flow, collectively called complex here, is such that an assumption of homogeneity in two or three spatial directions may not be made, classic linear theory cannot be applied. Interesting flow phenomena arising either on account of geometrical complexity, e.g. flow over protrusions, corners, steps or gaps, or because of the interaction of a shock system with a laminar boundary layer over a flat plate or a (plane or axisymmetric) wedge, all are beyond the scope of classic linear stability theory. While the above is already true for supersonic flow, the hypersonic regime further

compounds the problem, since as mentioned chemical reactions and their modeling need to be taken into account. To-date, when laminar-turbulent transition of a complex flow field need to be studied, one resorts to state-of-the-art direct numerical simulation [9, 18]. It is worth to mention that [7, 14] studied also the effect of finite-rate chemistry or non-equilibrium chemistry adding some equations for species conservation in the classic local stability analysis of flat-plate boundary layers.

The present contribution discusses algorithmic developments to include real gas effects in stability equations without any restriction on spatial homogeneity. The phrase *real gas* is used in the sense of aerodynamics where it typifies the high-temperature effects rather than in the sense of classical physical chemistry where it has been used for a gas in which inter-molecular forces are important due to high pressures and/or low temperatures. The problem considered is the hypersonic flow over a backstep in chemical equilibrium where the five species model proposed by Park [11], which is valid up to 9000 K, is considered in the last case. This model becomes invalid when the ionization of atoms start. These results are compared with the results obtained when perfect gas approximation is considered, where internal energy and enthalpy are functions of the temperature only. Before to this, verification is performed against spatial local stability results of Malik and Anderson [8] in a zero-pressure-gradient flat-plate boundary layer at Mach 10. In this way, the chemical model and inflow profile for the solution of the backstep base flow are validated.

2. Problem description

The governing equations used are the time-dependent three-dimensional Navier-Stokes equations for compressible fluids in dimensional form,

$$\frac{\partial \rho^*}{\partial t} + \nabla \cdot (\rho^* \mathbf{u}^*) = 0, \tag{2.1}$$

$$\rho^* \left[\frac{\partial \mathbf{u}^*}{\partial t} + (\mathbf{u}^* \cdot \nabla)\mathbf{u}^* \right] = -\nabla p^* + \nabla[\lambda^*(\nabla \cdot \mathbf{u}^*)]$$
$$+ \nabla \cdot [\mu^*((\nabla \mathbf{u}^*) + (\nabla \mathbf{u}^*)^{\mathbf{T}})], \tag{2.2}$$

$$\rho^* \left[\frac{\partial e^*}{\partial t} + (\mathbf{u}^* \cdot \nabla)e^* \right] + p^* \nabla \mathbf{u}^* = \nabla \cdot (\kappa^* \nabla T^*)$$
$$+ \lambda^*(\nabla \cdot \mathbf{u}^*)^{\mathbf{2}} + \frac{\mu^*}{\mathbf{2}}[(\nabla \mathbf{u}^*) + (\nabla \mathbf{u}^*)^{\mathbf{T}}]^{\mathbf{2}}, \tag{2.3}$$

where $\mathbf{u}^*$ is the velocity vector, ρ^* the density, p^* the pressure, T^* the temperature, $e^* = c_v^* T^*$ the internal energy, κ^* the thermal conductivity, μ^* the first coefficient of viscosity, and λ^* the second coefficient of viscosity. Note that using the Stoke's law $\lambda^* = -2/3\mu^*$ and the asterisk denotes dimensional quantities.

The Cartesian coordinates are denoted by x, y, and z to represent the streamwise direction and the perpendicular plane to it, the normal and spanwise directions, respectively. The non-dimensionalization is based on the freestream conditions. Lengths are scaled by a reference length l_r^* defined as the Blasius length at x_h, velocity by U_r^* and temperature by T_r^* are defined from the boundary-layer edge at the step position. The reference pressure is p_r^*, the free-stream sound speed is denoted by s_r^*, and $\gamma = c_{p,r}^*/c_{v,r}^*$. The equation of state is given by the perfect gas relation $p^* = \rho^* \mathcal{R} T^*$, where $\mathcal{R}$ is the gas constant, which depends on the chemical composition of the gas. The resulting dimensionless parameters are the Reynolds number, $Re = \rho_r^* U_r^* l_r^*/\mu_r^*$,
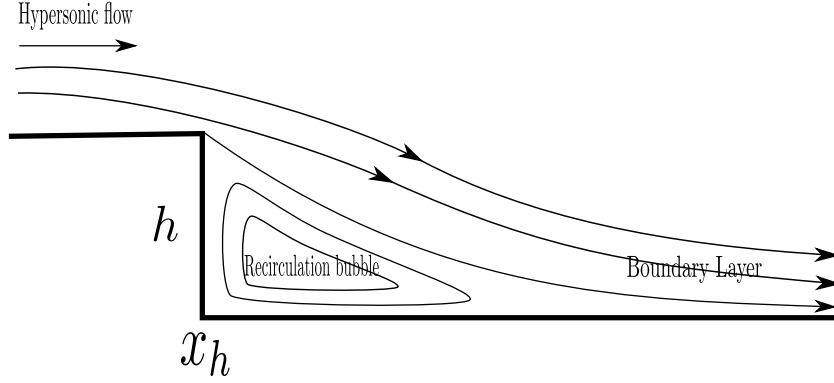
FIGURE 1. Flow geometry for the backstep.

the Prandtl number to $Pr = c_{p,r}^* \mu_r^* / \kappa_r^*$, the Mach number $M = U_r^* / s_r^*$ and the Eckert number $Ec = (U_r^*)^2 / (c_{p,r}^* T_r^*) = (\gamma - 1) M^2$.

2.1. *Compressible fluid properties*

2.1.1. *Perfect gas*

When a perfect gas is considered, the non-dimensionalized equation of state is

$$p = \frac{1}{\gamma M^2} \rho T \qquad (2.4)$$

where the constant of perfect gases is fixed to $\gamma = 1.4$ and the Prandtl number $Pr = 0.7$. The Sutherland's law is used for the viscosity coefficient

$$\mu = (T)^{3/2} \frac{1 + S}{T + S} \qquad (2.5)$$

with $\mu_s^* = 1.716 \times 10^{-5}$ N s/m² and $S = 110.4$ K$/T_r^\star$ for air in standard conditions. The dimensionless thermal conductivity of the medium is taken equal to the viscosity coefficient $\bar{\kappa} = \bar{\mu}$.

2.1.2. *Real gas*

At certain flight conditions, mostly as a cause of high temperature, some molecular species begin to dissociate due to aerodynamic heating and the perfect gas assumption is no longer applicable and real gas effects need to be considered. Air cannot be modeled as a perfect gas when vibrational excitation and chemical dissociation become important. At pressure of 1 atmosphere, oxygen starts dissociating at 2000 K, Nitrogen starts to dissociate at 4000 K and both atomic components start ionizing at about 9000 K. The equation of state for a real gas depend on its chemical composition. In addition, the internal energy, viscosity laws and thermal conductivity coefficients are not solely dependent on the temperature, but on the two thermodynamic variables considered.

Here, the gas properties, p^*, e^*, κ^* and μ^* as function of ρ^* and T^* are calculated using the TAU software. Air of 5 species, namely N_2, O_2, NO, N and O, is considered next. Comparison with perfect gas is shown in Figure 2. The divergence of the gas properties for perfect and real gas is evident as the temperature increases. p^* and μ^* for perfect gas start to deviate from the real gas solution at about $T^* \approx 2000$ K, while differences for e^* and κ^* are visible above $T^* \approx 1000$ K.
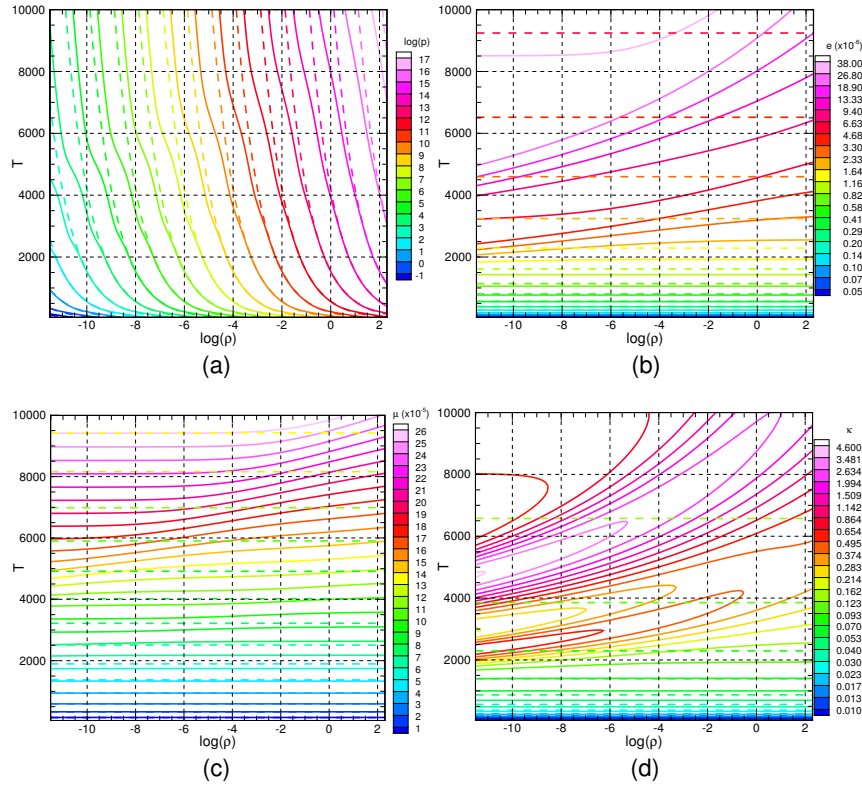
FIGURE 2. (a) $\log(\bar{p})$ (log(kg m/s^2)), (b) $\bar{e}$ (J/kg), (c) $\bar{\mu}$ (kg/(m s)) and (d) $\bar{\kappa}$ (W/(m K)). Note that (a) and (c) are plotted using a constant increment between iso-lines, while (b) and (d) use an exponential increase of intervals between iso-lines.
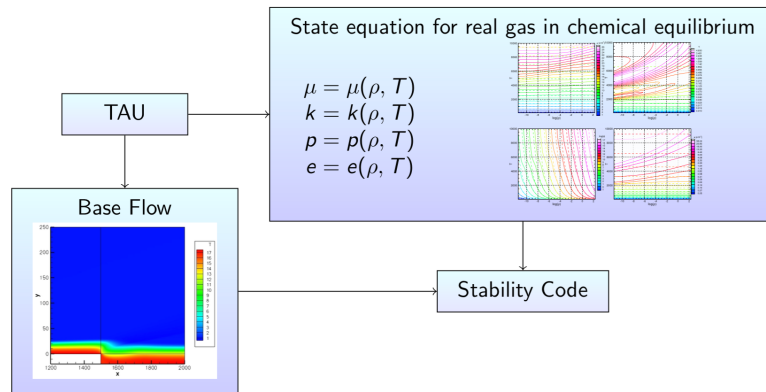

FIGURE 3. Procedure followed in the stability analysis in the case of real gas calculation. As it can be seen TAU provides both the base flow and the database used in the calculation of the unknowns thermodynamic variables and coefficients.

In this work, gas properties provided by TAU are tabulated, and Lagrange interpolation is used to obtain the desired values for the stability analysis. Figure 3 shows the process followed in the stability analysis when real gas is considered. Basically TAU provides the base flow and some tables that are used by the stability code in order to calculate the value of the thermodynamic variables and parameters for a real gas in thermal and chemical equilibrium.

Once this information is available the next step requires the solution of the eigenvalue problem associated with the modal stability analysis. To do this, a zoom near the step is considered and the domain is splited into three domains. A $\mathcal{C}^1$ condition is imposed at the connection between the different domains.

3. Hydrodynamic stability theory

3.1. *Linearized Navier-Stokes equations*

The vector of fluid variables $\mathbf{q} = (\rho, u, v, w, T)^T$ is decomposed into a steady mean flow $\bar{\mathbf{q}}$ and an unsteady small disturbance or perturbation $\tilde{\mathbf{q}}$:

$$\mathbf{q}(\mathbf{x}, t) = \bar{\mathbf{q}}(\mathbf{x}) + \epsilon\tilde{\mathbf{q}}(\mathbf{x}, t), \quad \epsilon \ll 1. \tag{3.1}$$

The amplitude functions of thermal conductivity and viscosity coefficients, internal energy and pressure are functions of temperature and density, and thus are written as

$$\tilde{\mu} = \bar{\mu}_T \tilde{T} + \bar{\mu}_R \tilde{\rho}, \tag{3.2}$$

$$\tilde{\kappa} = \bar{\kappa}_T \tilde{T} + \bar{\kappa}_R \tilde{\rho}, \tag{3.3}$$

$$\tilde{e} = \bar{e}_T \tilde{T} + \bar{e}_R \tilde{\rho}, \tag{3.4}$$

$$\tilde{p} = \bar{p}_T \tilde{T} + \bar{p}_R \tilde{\rho}, \tag{3.5}$$

where $()_T = \frac{\partial()}{\partial\bar{T}}$, $()_R = \frac{\partial()}{\partial\bar{\rho}}$. Also, second order derivatives with respect to temperature and density arise from the spatial derivatives of previous thermodynamic variables. For example the x-derivative of viscosity coefficient is written as

$$\frac{\partial\tilde{\mu}}{\partial x} = \left(\bar{\mu}_{TT}\bar{T}_x + \bar{\mu}_{RT}\bar{\rho}_x + \bar{\mu}_T\frac{\partial}{\partial x}\right)\tilde{T}, \tag{3.6}$$

$$+ \left(\bar{\mu}_{RT}\bar{T}_x + \bar{\mu}_{RR}\bar{\rho}_x + \bar{\mu}_R\frac{\partial}{\partial x}\right)\tilde{\rho}, \tag{3.7}$$

where $()_{TT} = \frac{\partial^2()}{\partial\bar{T}^2}$, $()_{RT} = \frac{\partial^2()}{\partial\bar{\rho}\partial\bar{T}}$ and $()_{RR} = \frac{\partial^2()}{\partial\bar{\rho}^2}$.

By introducing the previous decomposition of variables (3.1) into the governing equations (2.1-2.3) and neglecting the non-linear terms of $\mathcal{O}(\epsilon^2)$ and $\mathcal{O}(\epsilon^3)$, the linearized Navier-Stokes equations (LNSE) are recovered.

The above generic discussion is applicable to any linearization of the governing equations following the decomposition of flow quantities (3.1). Furthermore, in modal linear stability theory, the perturbation term is usually written as the product of an amplitude function and a phase function, $\tilde{\mathbf{q}} = \hat{\mathbf{q}}\Theta$. Table 1 summarizes the different instability approaches arranged by increasing constraints to the basic flow. However, depending on the dimensionality of the base flow analyzed, the resulting theoretical frameworks involve numerical solutions that require orders-of-magnitude different levels of computational work for their solution.

The best known context of *classic* or *local* linear stability theory [6] assumes a single

	Assumptions	Base	Amplitude	$Exp(i\Theta)$, Phase Function Θ
TriGlobal	-	$\overline{\mathbf{q}}(x,y,z)$	$\hat{q}(x,y,z)$	$-\omega t$
PSE-3D	$\partial_z\overline{\mathbf{q}} \ll \partial_x\overline{\mathbf{q}}, \partial_y\overline{\mathbf{q}}$	$\overline{\mathbf{q}}(x,y,z^*)$	$\hat{q}(x,y,z^*)$	$\int \beta(z')dz' - \omega t$
BiGlobal	$\partial_z\overline{\mathbf{q}} = 0$	$\overline{\mathbf{q}}(x,y)$	$\hat{q}(x,y)$	$\beta z - \omega t$
PSE	$\partial_x\overline{\mathbf{q}} \ll \partial_y\overline{\mathbf{q}}$ $\partial_z\overline{\mathbf{q}} = 0$	$\overline{\mathbf{q}}(x^*,y)$	$\hat{q}(x^*,y)$	$\int \alpha(x')dx' + \beta z - \omega t$
Local	$\partial_x\overline{\mathbf{q}} = \partial_z\overline{\mathbf{q}} = 0$	$\overline{\mathbf{q}}(y)$	$\hat{q}(y)$	$\alpha x + \beta z - \omega t$

TABLE 1. Modal linear instability approaches arranged by increasing constraints to the basic flow

in-homogeneous spatial direction in both the basic flow and the amplitude functions, indicated by y in the last line of Table 1. On the other hand, the linear (and non-linear) stability of boundary-layer flows, in which a small but non-zero wall-normal velocity component exists in the base flow and the dependence of the latter on the streamwise coordinate, x, is much weaker than that along the wall-normal, y, can be studied by the Parabolized Stability Equations (PSE). Unlike an EVP-based solution, PSE solve a marching integration of the LNSE along the streamwise spatial direction, and is known as a *non-local* instability analysis; [3] provides an introduction to the PSE. The remaining three entries in Table 1 are collectively known as *global* linear theories [16]. They may consider base flows which are inhomogeneous in two or three (rather than one) spatial directions. The global stability theories are classified in BiGlobal, PSE-3D and TriGlobal analysis. They denote analysis of base flows developing in two (BiGlobal) or three (TriGlobal) inhomogeneous spatial directions. In-between, the PSE-3D concept extends the classic PSE to flows depending strongly on two and weakly on the third spatial direction.

3.2. *Temporal and spatial stability analysis*

The aforementioned LNSE can be written as initial-value-problem (IVP) in the form

$$\mathcal{B}_T \frac{\partial \tilde{\mathbf{q}}}{\partial t} = \mathcal{A}_T \tilde{\mathbf{q}}, \tag{3.8}$$

and solutions to this system of PDEs are considered. The operators $\mathcal{A}$ and $\mathcal{B}$ are associated with the spatial discretization of the LNSE and comprise the basic state, $\overline{\mathbf{q}}(\mathbf{x})$ and its spatial derivatives and the thermodynamic properties of the gas. In case of steady basic flows, the separability between time and space coordinates in (3.8) permits introducing a Fourier decomposition in time through the expression $\tilde{\mathbf{q}} = \hat{\mathbf{q}}\exp(-\mathrm{i}\omega t)$, where $\hat{\mathbf{q}} = (\hat{\rho}, \hat{u}, \hat{v}, \hat{w}, \hat{T})^T$ is the vector of amplitude functions, leading to the generalized matrix eigenvalue problem (EVP)

$$\mathbf{A}_T \hat{\mathbf{q}} = \omega \mathbf{B}_T \hat{\mathbf{q}}, \tag{3.9}$$

in which matrices $\mathbf{A}_T$ and $\mathbf{B}_T$ discretize the operators $\mathcal{A}_T$ and $\mathcal{B}_T$, respectively, and incorporate the boundary conditions. This EVP represents a modal temporal stability

problem in which the sought complex eigenvalue is $\omega = \omega_r + \mathrm{i}\omega_i$, the real part being a circular frequency, while the imaginary part is the temporal amplification/damping rate.

In certain problems, the study of the spatial development of perturbations is considered instead. In such cases, at least one homogeneous direction is assumed and the disturbances obey the wave-like ansatz $\exp[\mathrm{i}(\beta z - \omega t)]$. Here, the IVP (3.8) is rewritten as

$$\mathcal{B}_S \frac{\partial \tilde{\mathbf{q}}}{\partial x} = \mathcal{A}_S \tilde{\mathbf{q}}, \tag{3.10}$$

and the discretized version becomes a quadratic generalized matrix EVP

$$\mathbf{A}_S \hat{\mathbf{q}} = \sum_{k=1}^{2} \beta^k \mathbf{B}_{S,k} \hat{\mathbf{q}}. \tag{3.11}$$

Here $\omega \in R$ is a real frequency parameter, while $\beta \in C$ is the sought eigenvalue, the real part of which is related with the periodicity length along the homogeneous spatial direction, x, through $\beta_r = 2\pi/L_z$ and the imaginary part, β_i is the spatial amplification/damping rate.

In order to solve numerically the quadratic EVP, it must be previously reduced to a linear EVP. The latter problem can be converted into a (larger by a factor equal to the degree of non-linearity) linear EVP, as shown by [15], using the companion matrix method [1], in which an auxiliary vector $\hat{\mathbf{q}}^* = [\hat{\rho}, \hat{u}, \hat{v}, \hat{w}, \hat{T}, \beta\hat{u}, \beta\hat{v}, \beta\hat{w}, \beta\hat{T}]^T$ is defined, resulting in

$$\mathbf{A}_S \hat{\mathbf{q}}^* = \beta \mathbf{B}_S \hat{\mathbf{q}}^*. \tag{3.12}$$

Matrices $\mathbf{A}_S$ and $\mathbf{B}_S$ defined in (3.12) and (3.11) are different.

4. Spatial analysis of flat-plate boundary-layer

The spatial stability analysis of a hypersonic flat-plate boundary-layer at Mach 10 is studied for verification purposes. This problem was selected by [8] to show the effects of considering real gas effects, assuming chemical equilibrium, in stability analysis. The objective is to validate the real gas calculation and the self-similarity solution that are used in the following section. The Mach 10 boundary-layer calculation is performed using either a self-similar boundary-layer code or the TAU software for the perfect gas and real gas cases, respectively. In both cases adiabatic wall condition is set. The boundary-layer edge temperature is $T_r^* = 350$ K and the unit Reynolds number is $Re' = 6.6 \times 10^6$ 1/m. The Re' affects the real gas properties through the reference pressure, which is implicitly calculated knowing T_r^*, M and Re'.

Boundary-layers profiles as function of the wall normal direction for perfect and real gas used for stability analysis are compared with those used by [8] in figure 4 at $x^\star \approx 0.606$ (or $R = 2000$). Figure 4 shows the streamwise velocity and temperature for both perfect and real flow approaches where the lengths are dimensionlalized by using l_r defined previously. $\delta^\star$ (boundary-layer thickness) is about 40 times l_r. In both cases there is a good agreement with Malik's results [8]. As it can be seen, there is a decrease in temperature of about 45% under the consideration of chemical reactions. Related with this, for boundary-layer flow over a flat plate wall temperature increases when the free-stream Mach number increases too. The following approximate equation relates these two parameters,

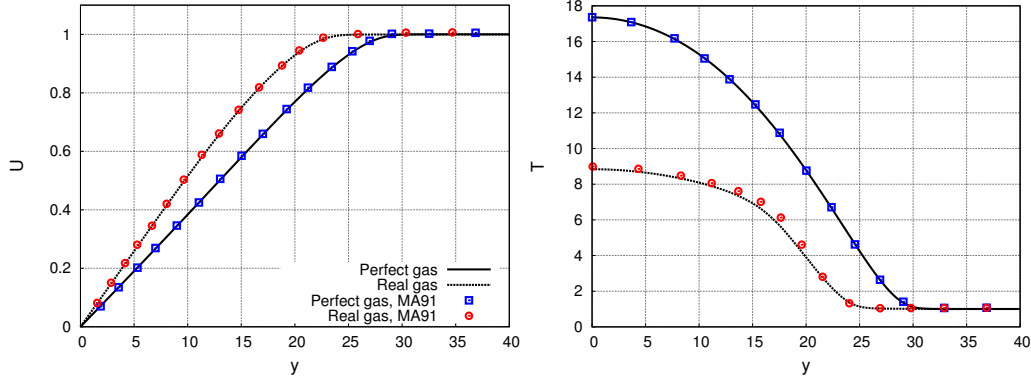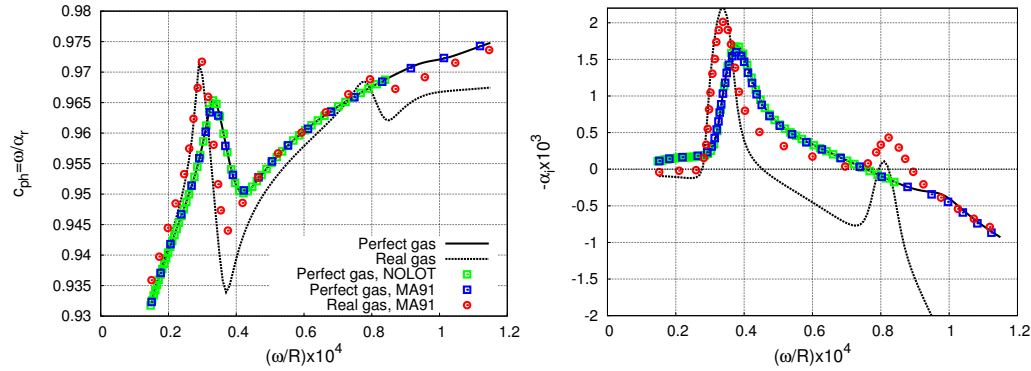$$T_{ad}^\star / T_r^\star = 1 + \frac{\gamma - 1}{2} \sqrt{Pr} M_r^2 \ .$$

FIGURE 4. (a) Streamwise velocity, (b) Temperature

FIGURE 5. Spatial local stability results of two-dimensional waves ($\beta = 0$). (a) Phase speed and (b) growth rate.

This relation assumes that the temperature profile across the boundary layer is only a function of the streamwise velocity. This is valid when the Prandtl number is one but it is a good approximation in other cases (see [10]).

Stability results obtained by using the base flows shown in Figure 4 are compared in Figure 5 for two-dimensional waves, i.e. second and third Mack modes [6]. As can be seen the growth rate and phase velocity of the second and third modes are recovered in reasonable agreement with results of Malik & Anderson [8]. The small differences found in the real case are thought to be due to the base flow used here, which has been computed using the full Navier-Stokes solution of a complete flat plate including the leading edge and shock wave, instead of the self-similar solution used in Ref. [8]. In this case x is the homogeneous direction and then α is the wavenumber considered in the ansatz. For the boundary layer on a flat plate, ω can be expressed as FR where $R = \sqrt{U_r^\star x^\star / \nu_r^\star}$ is the Reynolds number, $F = \omega \nu_r^\star / (U_r^\star)^2$ is the frequency parameter and ω is the frequency of the spatial perturbation. In Figure 5 the first of the higher modes, which was labeled as the second mode by Mack, has been found to be the dominant unstable mode for a zero-pressure-gradient boundary layer over a flat plate at high Mach numbers. This study also shows that the third mode, which did not appear in the perfect gas analysis, is marginally unstable too.
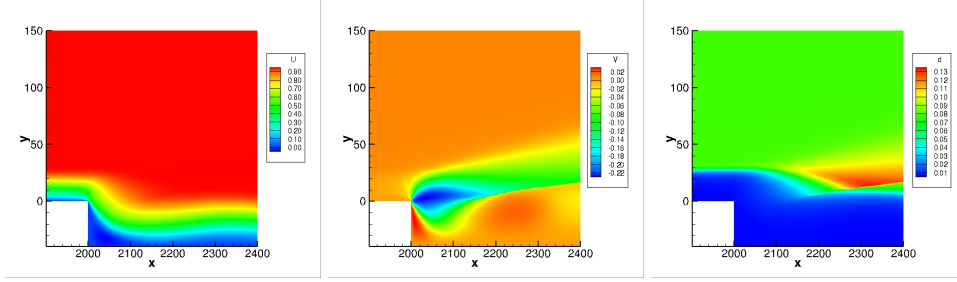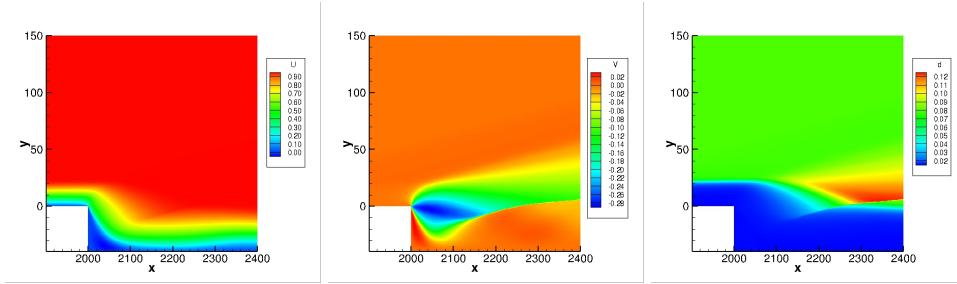
FIGURE 6. Base flow at $M = 10$, $Re = 2000$, $T_r = 350$ K, $L_r = R/Re' = 3 \times 10^{-4}$ m and $h = \delta^\star$ obtained by using the approximation of perfect gas. (*left*) Streamwise velocity (*center*) wall-normal velocity (*right*) and density.

FIGURE 7. Base flow at $M = 10$, $R = 2000$, $T_r = 350$ K, $L_r = R/Re' = 3 \times 10^{-4}$ m and $h = \delta^\star$ obtained by using the approximation of real gas. (*left*) Streamwise velocity (*center*) wall-normal velocity (*right*) and density.

5. Temporal analysis of backstep boundary-layer

Temporal linear instability over the backstep boundary layer flow is considered in this section. In these simulations the self-similar boundary-layer solution obtained in the previous section (see Figure 4) is prescribed at the inflow. Boundary conditions at the wall are no-slip, non-catalytic, and adiabatic, while non-reflecting boundary conditions are used at the far-field and outflow boundaries.

Figures 6 and 7 show the streamwise velocity, wall normal velocity and density of the base flow for perfect and real gas approaches, respectively. Figure 8 shows the recirculation bubble in both configurations. In the latter case the recirculation level is lower than in the former. This aspect is not crucial when analyzing convective 2D and 3D modal instabilities, which may be present even at zero-recirculation, but it should be taken into consideration when analyzing global 3D instabilities of the entire recirculation zone, for which a recirculation level of $\approx 10\%$ is known to be necessary in incompressible flow [12, 17]; analogous studies in hypersonic separated flow have to-date not been performed.

A convergence study of the base flow in the recirculation region is shown in Figure 9. The first figure shows the streamwise velocity as function of the wall normal direction obtained at different resolutions in the recirculation bubble. The other figure shows the temperature as function of the wall normal direction. In both cases there is a good agreement between the data obtained at different resolutions. Finally as can be seen in Figure 10 chemical equilibrium destabilizes the dominant leading mode which is a global mode defined in the recirculation bubble.
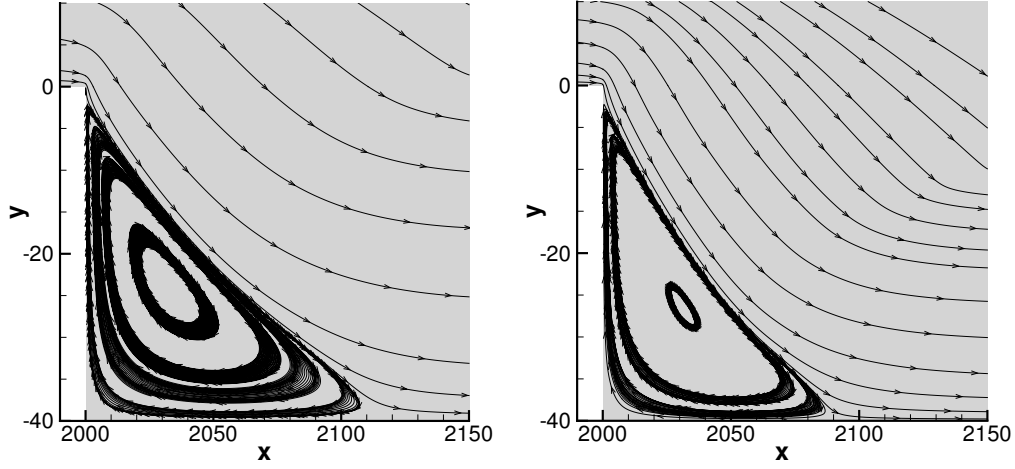
FIGURE 8. Recirculation bubbles at $M = 10$, $R = 2000$, $T_r = 350$ K, $L_r = R/Re' = 3 \times 10^{-4}$ m and $h = \delta^\star$. (*left*) Perfect gas and (*right*) real gas. In both cases the recirculation level, $|u_{max}|/|u_{min}|100$, is about 7%.
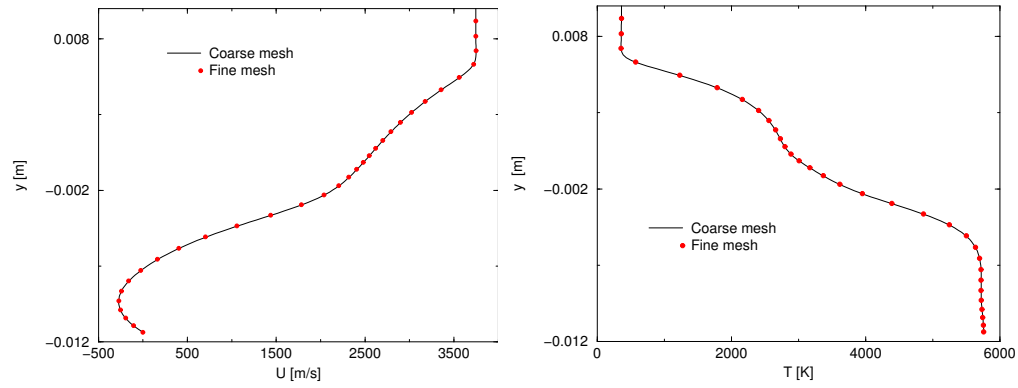

FIGURE 9. Convergence of the base flow inside the recirculation bubble ($h = 1/2\delta^\star$) and dimensional x position of 0.3. Streamwise velocity and temperature as a function of the wall-normal distance.

A convergence study of the leading eigenmodes was also performed in order to ensure the good resolution of this mode. The module of the amplitude functions for the velocity and temperature are shown in Figure 11 and 12 for perfect and real gas, respectively. The modulus of the streamwise and wall-normal velocity components and temperature of the leading mode using both approaches, i.e., perfect and real gas, are qualitatively similar with a small deformation due to the base flow modification. This identification allows to identify both modes as the same modal instability.

References

[1] T.J. Bridges and P.J. Morris. Differential eigenvalue problems in which the parameter appears nonlinearly. *J. Comp. Phys.*, 55:437–460, 1984.

[2] A. Demetriades. Hypersonic viscous flow over a slender cone, part iii: laminar instability and transition. *AIAA Astronaut. Fluid Plasma Dyn. Conf., 7th, Palo Alto,*
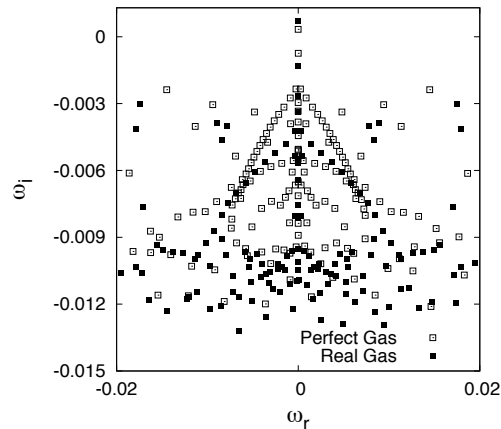
FIGURE 10. Comparison of the spectra obtained with real and perfect gas approaches at $M = 10$, $Re = 2000$, $T_r = 350$ K, $L_r = R/Re_1 = 3 \times 10^{-4}$ m, $h = \delta^\star$ and dimensional x position of 0.606.

CA, AIAA Pap., page 535, 1945.

[3] T. Herbert. Parabolized stability equations. *Ann. Rev. Fluid Mech.*, 29:245–283, 1997.

[4] M. R. Khorrami. Wind tunnel experiments relating to supersonic and hypersonic boundary layer transition. *AIAA Journal*, 13(3):290–299, 1975.

[5] L. Mack. Boundary layer stability theory. Technical report, JPL Report 900-277, Jet Propulsion Laboratory, California Institute of Technology, Pasadena, CA, USA, 1969.

[6] L. M. Mack. Boundary layer linear stability theory. In *AGARD–R–709 Special course on stability and transition of laminar flow*, pages 3.1–3.81, 1984.

[7] M. R. Malik. Prediction and control of transition in hypersonic boundary layers. AIAA Paper 87-1414, 1987.

[8] M. R. Malik and E. C. Anderson. Real gas effects on hypersonic boundary-layer stability. *Phys. Fluids A*, 3(5):803–821, 1991.

[9] O. Marxen, G. Iaccarino, and E. S. G. Shaqfeh. Disturbance evolution in a mach 4.8 boundary layer with two-dimensional roughness-induced separation and shock. *J. Fluid Mech.*, 648:435–469, 2010.

[10] J. A. Masad and R. Abid. On transition in supersonic and hypersonic boundary layers. *Int. J. Engng Sci.*, 33(13):1893–1919, 1995.

[11] C. Park. On convergence of chemical reacting flows. *AIAA Paper*, page 0427, 1985.

[12] D. Rodríguez and V. Theofilis. Structural changes of laminar separation bubbles induced by global linear instability. *J. Fluid Mech.*, 655:280–305, 2010.

[13] K.F. Stetson and R.L. Kimmel. On hypersonic boundary-layer stability. *AIAA Aerosp. Sci. Meet. Exhib., 30th, Reno, AIAA Pap.*, page 0737, 1992.

[14] G. Stuckert and H. Reed. Linear disturbances in hypersonic, chemically reacting shock layers. *AIAA J.*, 32:1384–1393, 1994.

[15] V. Theofilis. Spatial stability of incompressible attachment-line flow. *Theor. Comp. Fluid Dyn.*, 7(3):159–171, 1995.

[16] V. Theofilis. Global linear instability. *Annu. Rev. Fluid Mech.*, 43:319–352, 2011.

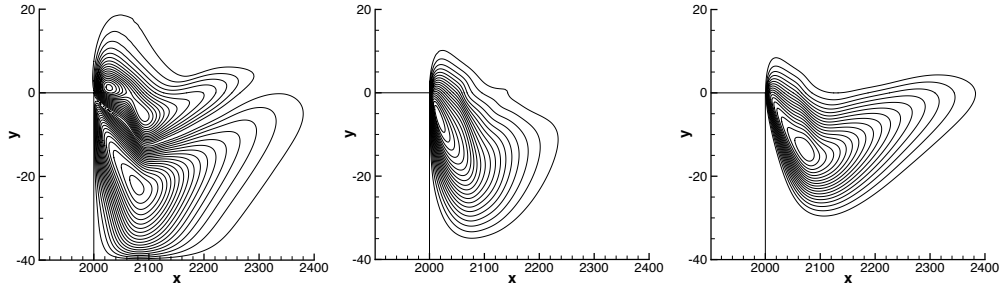[17] V. Theofilis, S. Hein, and U.Ch. Dallmann. On the origins of unsteadiness and

FIGURE 11. Amplitude of leading mode at $M = 10$, $Re = 2000$, $T_r = 350$ K, $L_r = R/Re_1 = 3 \times 10^{-4}$ m, $h = \delta^\star$ and $\beta = 2\pi/\delta^\star = 0.1571$ obtained by using the approximation of perfect gas. Module of the (*left*) streamwise amplitude velocity (*center*) wall-normal amplitude velocity (*right*) and amplitude temperature.
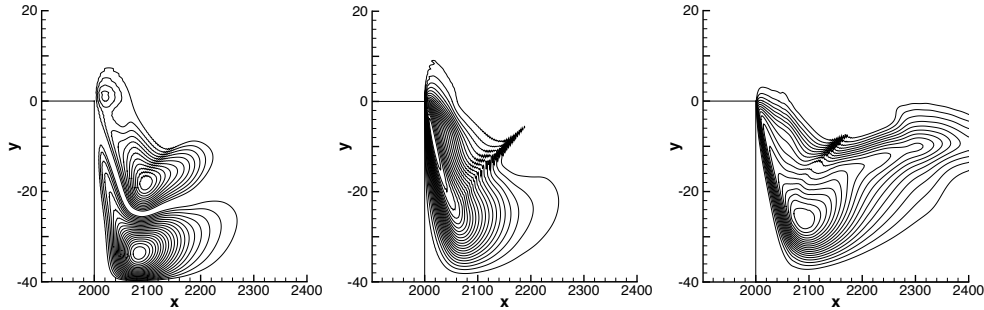

FIGURE 12. Amplitude of leading mode at $M = 10$, $Re = 2000$, $T_r = 350$ K, $L_r = R/Re_1 = 3 \times 10^{-4}$ m, $h = \delta^\star$ and $\beta = 2\pi/\delta^\star = 0.1571$ obtained by using the approximation of real gas. Module of the (*left*) streamwise amplitude velocity (*center*) wall-normal amplitude velocity (*right*) and amplitude temperature.

three-dimensionality in a laminar separation bubble. *Phil. Trans. Roy. Soc. London (A)*, 358:3229–324, 2000.

[18] X. Zhong. Additive semi-implicit runge-kutta methods for computing high speed non-equilibrium reactive flows. *J. Comp. Phys.*, 128:19–31, 1996.